

Constraints on localized core-mantle boundary structure from multichannel, broadband *SKS* coda analysis

Stéphane Rondenay¹ and Karen M. Fischer

Department of Geological Sciences, Brown University, Providence, Rhode Island, USA

Received 25 March 2003; revised 27 August 2003; accepted 17 September 2003; published 22 November 2003.

[1] In recent years, a wide range of geophysical results have offered evidence that Earth's lowermost mantle is characterized by strong lateral variations in material properties. Among the structures of particular interest are intermittent ultralow-velocity zones (ULVZs), located directly above the core-mantle boundary (CMB), which were originally inferred from the distortion of teleseismic *SPdKS* phases. ULVZs have been modeled as layers with sharp boundaries and seismic velocity reductions $\geq 10\%$ and interpreted as regions of partial melt. In this study, we further constrain local ULVZ structure beneath North America by signal processing and waveform modeling of the *SKS* coda recorded at broadband seismic arrays. Secondary phases in the *SKS* coda are effectively isolated by eigenimage processing. Residual (i.e., *SKS*-less) data sections from various western Pacific events display clear *SPdKS* arrivals, followed by a secondary phase whose timing and slowness are consistent with CMB origins. One-dimensional modeling of these phases by reflectivity and generalized ray synthetics favors an asymmetric model, with ULVZ present at only one of the CMB intercepts. The preferred ULVZ is characterized by reductions in *P* and *S* velocities of 18% and 50%, respectively, and a diffuse upper boundary. These characteristics are consistent with local production and gravitational sinking of dense (e.g., iron rich) partial melt above the CMB. We postulate that a gradational ULVZ beneath North America may mark a lateral transition domain between regions of mantle upwelling, where more uniform ULVZs exist, and regions of downwelling, where ULVZs are either nonexistent or imperceptibly thin. **INDEX TERMS:** 7207 Seismology: Core and mantle; 7260 Seismology: Theory and modeling; 8124 Tectonophysics: Earth's interior—composition and state (1212); **KEYWORDS:** lower mantle, CMB, broadband *SKS* coda, multichannel processing

Citation: Rondenay, S., and K. M. Fischer, Constraints on localized core-mantle boundary structure from multichannel, broadband *SKS* coda analysis, *J. Geophys. Res.*, 108(B11), 2537, doi:10.1029/2003JB002518, 2003.

1. Introduction

[2] An ever increasing body of seismological, geodynamical, and experimental evidence points to the core-mantle boundary (CMB) region as a zone which is characterized by strong lateral variations in physical and compositional properties. These variations occur at a variety of scales, ranging from degree 2–3 spherical harmonics in the lower 300 km (i.e., D'' layer) [e.g., Liu and Dziewonski, 1998; Masters et al., 2000] to kilometer-scale, local boundary layers situated at or just beneath the CMB [Rost and Revenaugh, 2001]. That such strong gradients may exist in this region is to be expected, as the CMB itself marks a major compositional and thermal discontinuity. Specifically, it separates the solid state convective lower mantle, composed primarily of perovskite and iron-magnesium oxides, from the liquid outer core, which is warmer and composed

primarily of iron. On the mantle side, the CMB may represent both the lower boundary where subducted plates end their descent [e.g., van der Hilst et al., 1998], and the source of ascending material that may or may not rise all the way into the upper mantle. On the core side, a recent study has shown that sedimentation of iron alloying elements may occur at regional scales along the CMB [Buffett et al., 2000]. Exchanges between the two domains are believed to take place through chemical reactions involving iron and high-pressure silicates [Knittle and Jeanloz, 1989]. Thermally, the CMB has been inferred to mark a ~ 1500 K superadiabatic gradient between the core and the lower mantle [Williams, 1998], contributing 10–15% of the surface heat flow.

[3] Seismological methods represent the principal tool for imaging structure in the CMB region. Common analyses focus on teleseismic body waves that interact with the CMB and normal mode data that are sensitive to lower mantle structure. Their results provide insight into seismic velocities, attenuation, mineral fabric, and topography at the CMB [e.g., Lay et al., 1998, and references therein].

[4] In recent years, the teleseismic body wave *SPdKS/SKPdS* has been extensively employed for CMB imaging

¹Now at the Department of Earth, Atmospheric and Planetary Sciences, Massachusetts Institute of Technology, Cambridge, Massachusetts, USA.

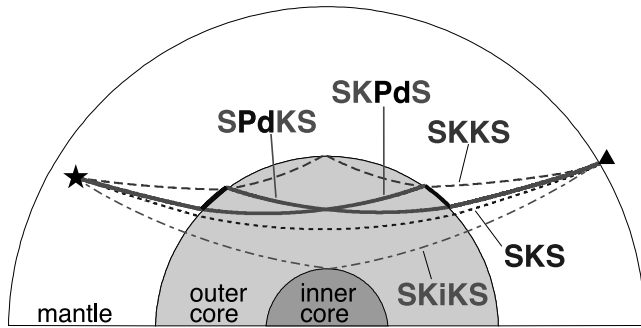


Figure 1. Ray geometry of teleseismic shear waves that illuminate the CMB. The phase *SPdKS-SKPds* is defined as an *SKS* wave which includes P_{diff} segments that sample velocities and structure directly above the CMB. Star, source location; triangle, receiver location.

purposes. This phase is defined as an *SKS* wave whose ray geometry includes a P_{diff} segment that travels along the CMB [e.g., Choy, 1977] (see Figure 1 and further discussion in section 2). By virtue of its characteristic path, the phase samples seismic velocities in the lowermost strata of the mantle. The systematic analysis of *SPdKS/SKPds* waveforms for imaging CMB structure was introduced by Garnero *et al.* [1993] [see also Garnero and Helmberger, 1995, 1996; Helmberger *et al.*, 1996]. This original study investigated rays which sampled the CMB beneath the central Pacific and displayed significant *SPdKS/SKPds* waveform distortions relative to signal expected for average, 1-D Earth models. These anomalous waveforms were successfully modeled with the addition of a finite layer of greatly reduced velocities above the CMB. Such basal layers have acquired the appellation of ultralow-velocity zones (ULVZs) and have been inferred to exist intermittently along the CMB.

[5] Using 1-D approaches, ULVZs have been generally modeled as 2–40 km thick layers with sharp boundaries and uniform seismic velocity reductions of $\delta V_p > 10\%$ for *P* waves and $\delta V_s > 30\%$ for *S* waves. Note that the intrinsic nature of the phases utilized in these approaches generally yields more robust constraints on δV_p than on δV_s [see, e.g., Garnero and Jeanloz, 2000]. The magnitude of δV_p and a preferred $\delta V_p:\delta V_s$ ratio of 1:3, established through the analysis of *PcP* precursors, have led to the suggestion that ULVZs represent layers of partial melt at the bottom of D'' [Williams and Garnero, 1996; Revenaugh and Meyer, 1997]. In addition, the global distribution of ULVZs has been correlated with regions of mantle upwelling [Garnero *et al.*, 1998] and the surface expression of mantle plumes [Williams *et al.*, 1998]. Wen and Helmberger [1998a] developed a hybrid method (generalized ray and finite difference) for modeling two-dimensional (2-D) CMB structure. They showed that certain perturbations in the *SKS-SPdKS* wave field may be explained by scattering from 250 to 400 km wavelength, ridge-shaped ULVZs. It is important to note that, in both 1-D and 2-D modeling schemes, significant trade-offs exist between the following ULVZ parameters [Garnero and Helmberger, 1998; Garnero and Jeanloz, 2000]: thickness, percent velocity and density anomaly, sharpness of bounding discontinuities,

and exact location of the layer relative to the CMB (i.e., core or mantle side). Further constraints on the existence and characterization of ULVZs have also been obtained through the analysis of *PKP* precursors [e.g., Wen and Helmberger, 1998b], and *ScP/PcP* core-reflected phases on stacked sections of short-period records [Mori and Helmberger, 1995; Revenaugh and Meyer, 1997; Rost and Revenaugh, 2001].

[6] To date, most *SPdKS/SKPds* studies have relied on long-period recordings from sparsely distributed permanent stations of the World-Wide Standardized Seismograph Network (WWSSN). In recent years, however, a marked increase in worldwide coverage of both permanent and temporary broadband stations has greatly improved our ability to record large numbers of high-quality *SPdKS/SKPds* waveforms. The main objective of this paper is to exploit these new, dense data sets and improve constraints on local ULVZ structure through multichannel analysis of *SKS* and *SPdKS/SKPds* waves. Two notable improvements are demonstrated in the study. First, the increase in spectral content sharpens the signal and allows for higher resolution in the modeling of CMB structure. Second, multichannel processing tools yield robust estimates of the *SKS* wavelet and powerful phase-stripping capabilities that enhance the observation of secondary phases in the *SKS* coda. These two improvements are illustrated in the paper through synthetic and observed data examples. We then present the analysis of teleseismic data recorded in North America by permanent stations of the IRIS Global Seismic Network (GSN) and the Canadian National Seismograph Network (CNSN), and portable stations of the Missouri to Massachusetts (MOMA) and Abitibi arrays. We proceed with 1-D waveform modeling of the North American data and conclude with the interpretation of the results in terms of local ULVZ structure.

2. *SPdKS-SKPds* Waves

[7] *SPdKS-SKPds* paths are illustrated in Figure 1. The P_{diff} segment of the ray samples velocities in the vicinity of the CMB, on both source (*SPdKS*) and receiver (*SKPds*) sides. For the remainder of this paper, we will use the general term *SPdKS* to describe both source- and receiver- side phenomena, specifying the exact side if necessary. The P_{diff} phase is generated when *SKS* intersects the CMB at a critical angle that corresponds to a null *S*-to-*P* transmission coefficient between mantle and core [e.g., Helmberger *et al.*, 1996]. This critical angle is dependent on the velocities of the media located on either side of the CMB. Therefore the onset of *SPdKS* occurs at a precise source-receiver epicentral distance which is tied to the critical angle. In 1-D mantle-side ULVZ models, the phase has a ray parameter (i.e., moveout, in rad/s) that is entirely defined by seismic velocities above the CMB:

$$p = \frac{R_{\text{cmb}}}{\alpha_{\text{cmb}}}, \quad (1)$$

where R_{cmb} is the radius of the CMB, and α_{cmb} is the *P* wave velocity sampled by the P_{diff} wave in the lowermost mantle.

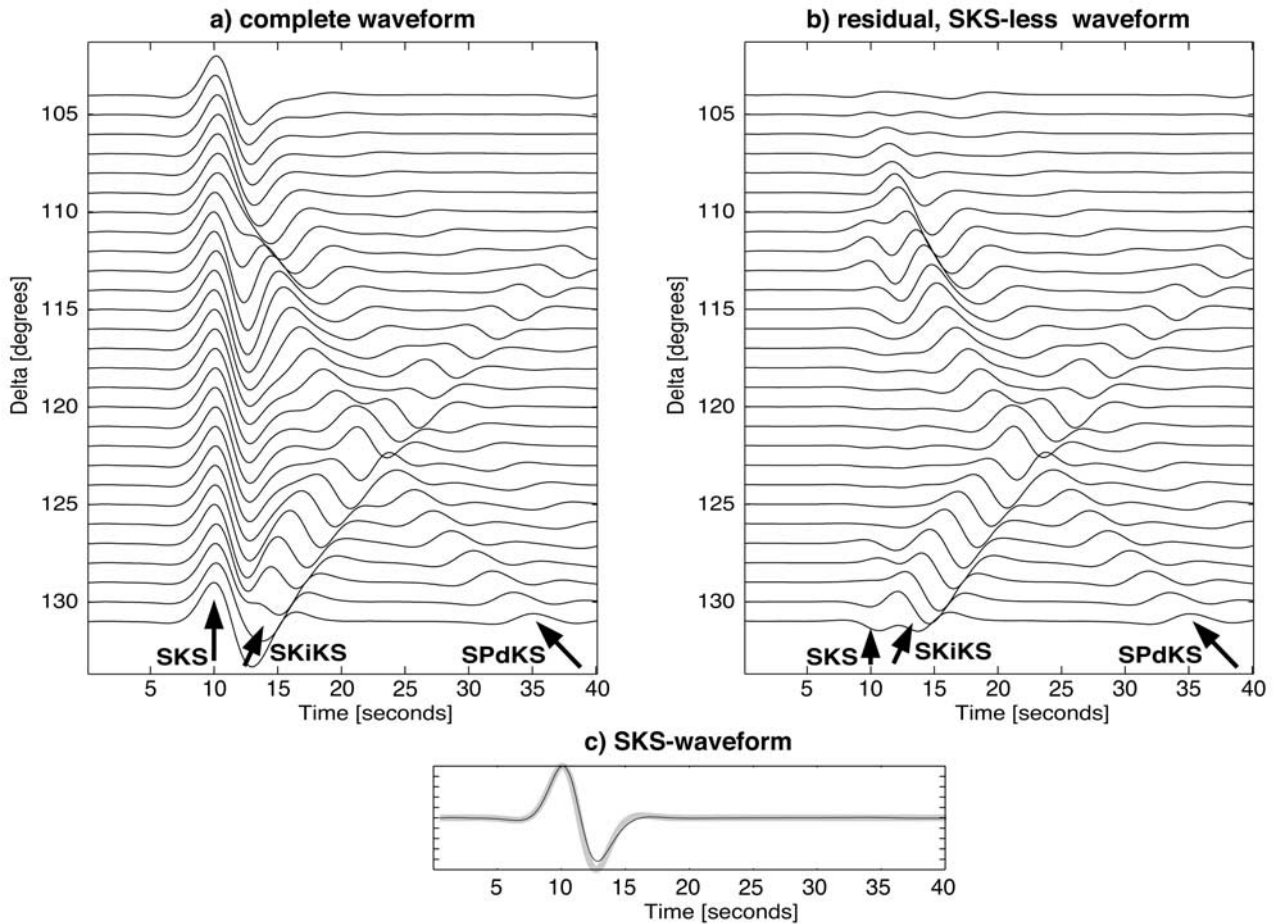


Figure 2. Synthetic data sections (i.e., velocity seismograms) obtained with the generalized ray method, for PREM architecture and a source depth of 600 km. The source time function is modeled with 1.6 s rise time and 2.0 s rupture time. Traces are normalized and aligned with respect to the main *SKS* pulse (centered at 10 s). (a) Complete waveform. (b) Residual waveform, where *SKS* has been effectively stripped from the section by eigenimage processing. The resulting section offers an unobstructed view of *SPdKS* and *SKiKS*, which remain unaffected by the processing. (c) Comparison between the input source time function (thick gray line) and the estimated *SKS* time function (thin black line), which corresponds the first eigenmode of Figure 2a.

[8] The characteristic *SKS-SPdKS* wave field is illustrated in Figure 2a, which shows radial synthetics produced with the generalized ray method [see, e.g., *Helmberger, 1983; Aki and Richards, 2002*] through the Preliminary Reference Earth Model (PREM [*Dziewonski and Anderson, 1981*]). Individual seismograms are represented as a function of station-event epicentral distance (in degrees) and time (in seconds), and all traces are aligned with respect to the *SKS* arrival at 10 s. Note that the traces presented here have been low-pass filtered with a corner frequency at 0.125 Hz (8 s), a value which reflects long-period data from WWSSN stations. *SPdKS* emerges as a distinct secondary pulse in the *SKS* coda near 110°. However, tau-*p* calculations through PREM indicate that the phase actually appears near 106°, where the ray parameter of *SKS* reaches the critical value of 4.43s/° (corresponding to PREM velocity $\alpha_{\text{cmb}} = 13.7$ km/s in equation (1)). The discrepancy between ray theoretical and modeled onsets of *SPdKS* is due, in large part, to the long period nature of the synthetics. Specifically,

this causes *SPdKS* to be obscured by the *SKS* wave field between 106 and 110°.

[9] The existence of ULVZs has been inferred from intermittent observations of distorted *SPdKS* waveforms relative to those predicted by PREM [*Garnero and Helmberger, 1995*]. On the basis of 1-D modeling work by *Garnero and Helmberger [1996, 1998]*, these distortions were interpreted as arising from (1) decoupling of source- and receiver-side *SPdKS* waves, and (2) constructive interference from multiple reverberations/conversions within the ULVZ. A synthetic example of distorted waveform is presented in Figure 3 for a source-side, 5 km thick ULVZ. The following perturbations in *P* velocity, *S* velocity, and density were used for this model: $\delta V_p = 10\%$, $\delta V_s = 30\%$, $\delta \rho = 0\%$. Note that the distortion includes a time shift of the apparent *SPdKS* arrival, which is associated with a smaller onset distance ($\sim 104^\circ$) than that observed for PREM ($\sim 110^\circ$). In field data, these anomalous *SPdKS* are observed only for rays sampling specific regions of the CMB,

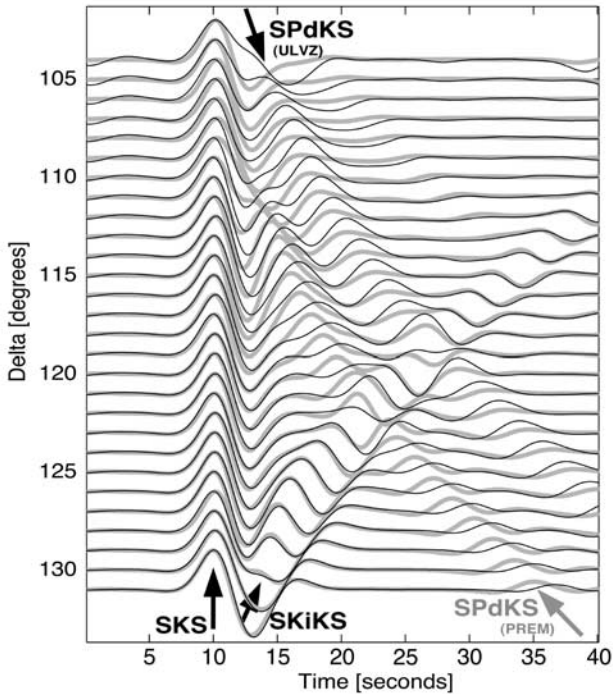


Figure 3. Generalized ray synthetics computed for PREM (thick gray lines) and a source-side ULVZ (thin black lines). Traces are normalized and aligned with respect to the main *SKS* pulse (centered at 10 s). ULVZ characteristics are thickness of 5 km, $\delta V_p = 10\%$, $\delta V_s = 30\%$, and $\delta \rho = 0\%$. The presence of an ULVZ distorts the *SPdKS* waveform, which emerges at smaller distances ($\sim 104^\circ$) and is observed later in the coda of *SKS*. Note that a PREM-like *SPdKS* is still observed in the distorted waveform, due to decoupling between source- and receiver-side *SPdKS*. Also note the presence of a small phase in the PREM waveforms, which is nearly coincident with the distorted *SPdKS*. This phase is a small, reproducible artifact of the method which is due to the discretization of the 1-D Earth model.

pointing to a lateral variability in ULVZ structure (see *Garnero et al.* [1998] for a review).

3. Data Processing

[10] Whereas early *SPdKS* analyses were limited to using records from sparsely distributed permanent stations, in recent years, broadband arrays have yielded denser spatial sampling equivalent to that in Figures 2 and 3. Consequently, data sections have become readily amenable to multichannel signal processing methods that can greatly facilitate the analysis of specific seismic phases. In this context, we introduce a signal processing algorithm that allows detailed analysis of the *SKS* coda by effectively stripping the *SKS* phase from the waveform, leaving any secondary phases (including *SPdKS*) nearly intact. The algorithm comprises three main steps, which are described below.

[11] First, all the traces from a single event are normalized relative to the maximum amplitude of the *SKS* pulse. Second, the traces are precisely aligned with respect to the *SKS* arrival using optimal delay times derived by multichannel cross correlation (i.e., estimated from cross-corre-

lation between each possible pair of traces [see *VanDecar and Crosson*, 1990]). The synthetic traces shown in Figure 2a are thus normalized and aligned. Third, the *SKS* signal is effectively stripped from the complete waveform by eigenimage (i.e., singular value) decomposition of the record section [Ulrych *et al.*, 1999]. The *SKS* waveform represents the signal that is most correlated from trace to trace and is thus estimated to be contained in the first eigenimage, which corresponds to the largest eigenvalue of the section. Following Ulrych *et al.* [1999], a residual (i.e., *SKS*-less) data section can be constructed by excluding the first eigenmode of the original section:

$$\mathbf{X}_R = \mathbf{U}_{2-n} \mathbf{U}_{2-n}^T \mathbf{X}, \quad (2)$$

where \mathbf{X} is the original $n \times m$ data section matrix containing n traces of m time samples (with, generally, $n \ll m$), and \mathbf{U}_{2-n} is an $n \times n$ matrix containing a column of zeros followed by the 2-to- n column eigenvectors of the covariance matrix $\mathbf{C} = \mathbf{X}\mathbf{X}^T$. Similarly, the first eigenimage is obtained through the following operation:

$$\mathbf{X}_1 = \mathbf{U}_1 \mathbf{U}_1^T \mathbf{X}, \quad (3)$$

where \mathbf{U}_1 is an $n \times n$ matrix whose first column is the only nonzero column and contains the first eigenvector of \mathbf{C} . Note that the eigenvectors in equations (2) and (3) must be sorted in order of decreasing magnitude of their corresponding eigenvalues. The residual section obtained in equation (2) preserves all the coherent phases whose moveouts differ from that of *SKS*. Alternatively, the first eigenimage (equation (3)) provides an estimate of the combined *SKS* and instrument time functions (hereafter referred to as “*SKS* estimate”) which can be used for modeling and deconvolution purposes.

[12] Figures 2b and 2c show the residual data section and *SKS* estimate obtained from the synthetic records of Figure 2a. The *SPdKS* wave has become a dominant phase in Figure 2b, with a pulse that is nearly devoid of *SKS* interference and an onset detected at smaller epicentral distances ($107-108^\circ$) than in the original section. Furthermore, this example shows that the processing algorithm also isolates *SKiKS*, which is distorted by *SKS-SPdKS* between 117 and 130° in the original section. Figure 2c shows a comparison between the *SKS* estimate and the synthetic source time function used to produce the original data section. The two traces are generally well correlated (correlation coefficient of 0.99), despite some noticeable discrepancies. The inability to perfectly recover the source time function is mainly due to variations in the *SKS* waveform over the sampled epicentral distance range. In particular, *SKS* waves propagating through PREM are inherently phase-shifted at distances $< 106^\circ$, as they intersect the CMB at supercritical incidence.

4. ULVZ Distribution

[13] In general, the process of locating ULVZs is hindered by the fundamental ambiguity that exists between source- and receiver-side intercepts of *SPdKS* at the CMB. Specifically, the geometry of *SPdKS* rays (see Figure 1) implies that either source- or receiver-side ULVZs produce identical

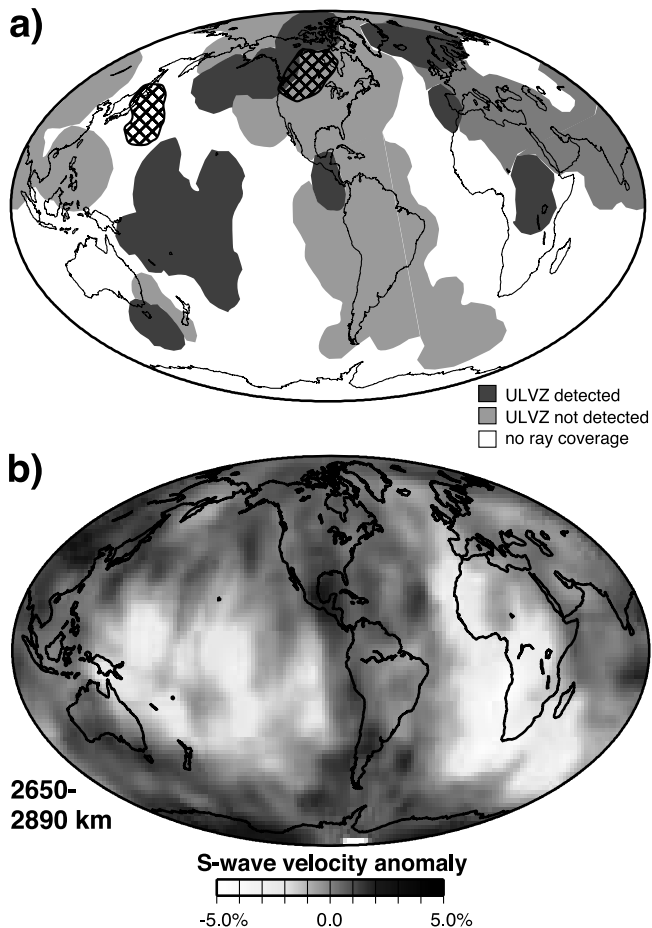


Figure 4. (a) Global ULVZ distribution inferred from previous teleseismic studies (modified from *Garnero et al.* [1998]). Outlined CMB regions in the northwestern Pacific and central North America are investigated here as possible sources for a secondary phase observed in the *SKS* coda. (b) A 3-D shear velocity model of the lowermost mantle (2650–2890 km depth) determined from global shear wave travel time tomography [*Grand, 2002*].

waveforms. This ambiguity can, however, be clarified by analyzing the correlations between responses from multiple source-receiver pairs and identifying CMB regions that consistently produce anomalous *SPdKS* [e.g., *Garnero and Helmberger, 1996*]. Using this approach, and including results from *ScP* and *PcP* precursors, a compilation map of global ULVZ distribution was generated by *Garnero et al.* [1998]. Figure 4 shows a modified version of this map, along with *S* velocity anomalies in the lowermost mantle from *Grand's* [2002] global tomographic model. Regions outlined in Figure 4a are defined by the Fresnel zones of the rays sampling the CMB. As noted by *Garnero et al.* [1998], ULVZs are predominantly detected in slow velocity regions believed to represent warmer temperatures and the base of mantle upwellings (e.g., central Pacific superplume). Conversely, regions of the CMB showing no evidence for ULVZs tend to be associated with faster than average velocities, probably related to colder temperatures in mantle/slab downwelling areas. Outlined areas in the northwestern Pacific and central North America (Figure 4a)

denote the CMB regions investigated in the following sections.

5. Analysis of North American Data

[14] In this section, we employ the eigenimage processing algorithm to investigate *SKS* data recorded at North American broadband stations. A total of 41 events sampling the CMB beneath North America were considered in this study; four of these were deemed representative of the entire data set and are reported here (see Table 1). Earthquakes were selected based on the following criteria: (1) sampled distance range between ~ 95 and 115° , in order to observe *SPdKS*, (2) magnitude $m_b > 6.0$ to ensure high signal-to-noise ratio (SNR) in the coda of *SKS*, and (3) intermediate to large focal depths, to minimize near-source scattering effects. For each event considered, a composite broadband array was formed by including portable stations from temporary deployments and permanent stations from the GSN and CNSN. To render the composite data sections amenable to eigenimage processing, the instrument response of each record was normalized to that of a generic Gralp CMG-3T broadband sensor.

5.1. Marianas, 23 August 1995

[15] For this first Marianas event (event 1 in Table 1), we analyze waveforms that were recorded in eastern North America by 18 portable stations of the Missouri to Massachusetts (MOMA) array [see, e.g., *Li et al., 2002*], and by permanent GSN stations CCM and HRV. The location of the stations and the theoretical *SKS-SPdKS* ray paths calculated for PREM are shown in Figure 5a. CMB intercepts along the ray paths are indicated either by a circle for *SKS* waves (i.e., distance $< 106^\circ$), or a thick line for *SPdKS* waves (i.e., distance $> 106^\circ$).

[16] Of the four events reported here, this is the one that generated the highest SNR in the *SKS* coda. We therefore use this example to illustrate the improvement in data resolution afforded by the broadband spectrum of the signal and eigenimage processing. Figure 6 shows a set of record sections from event 1, where all the traces are normalized and aligned relative to the *SKS* arrival, which is centered at 5 s. The first section (Figure 6a) shows the complete waveform low-pass filtered with cutoff frequencies at 0.015 Hz (i.e., 8 s period), which corresponds to the characteristic spectrum of long-period WWSSN data. The long-period section shows no clear evidence for *SPdKS* in the epicentral distance range 103 – 110° . A clear improvement in resolution occurs by increasing the spectral content of the signal, as illustrated in Figure 6b (see also Figure 7a) for cutoff frequency at 1.5 Hz. This has the effect of sharpening the *SKS* arrival and revealing *SPdKS* as a shoulder to *SKS* near 110° .

Table 1. Events Recorded at North American Stations

Event	Date	Time, UT	Latitude $^\circ$ N	Longitude $^\circ$ E	Depth, km	m_b
1	23 Aug. 1995	0706:04	18.81	145.23	614	7.1
2	16 March 1996	2204:07	28.97	138.98	482	6.4
3	9 June 1996	0112:19	17.32	145.71	167	6.0
4	23 April 2000	0927:23	-28.31	-62.99	609	6.6

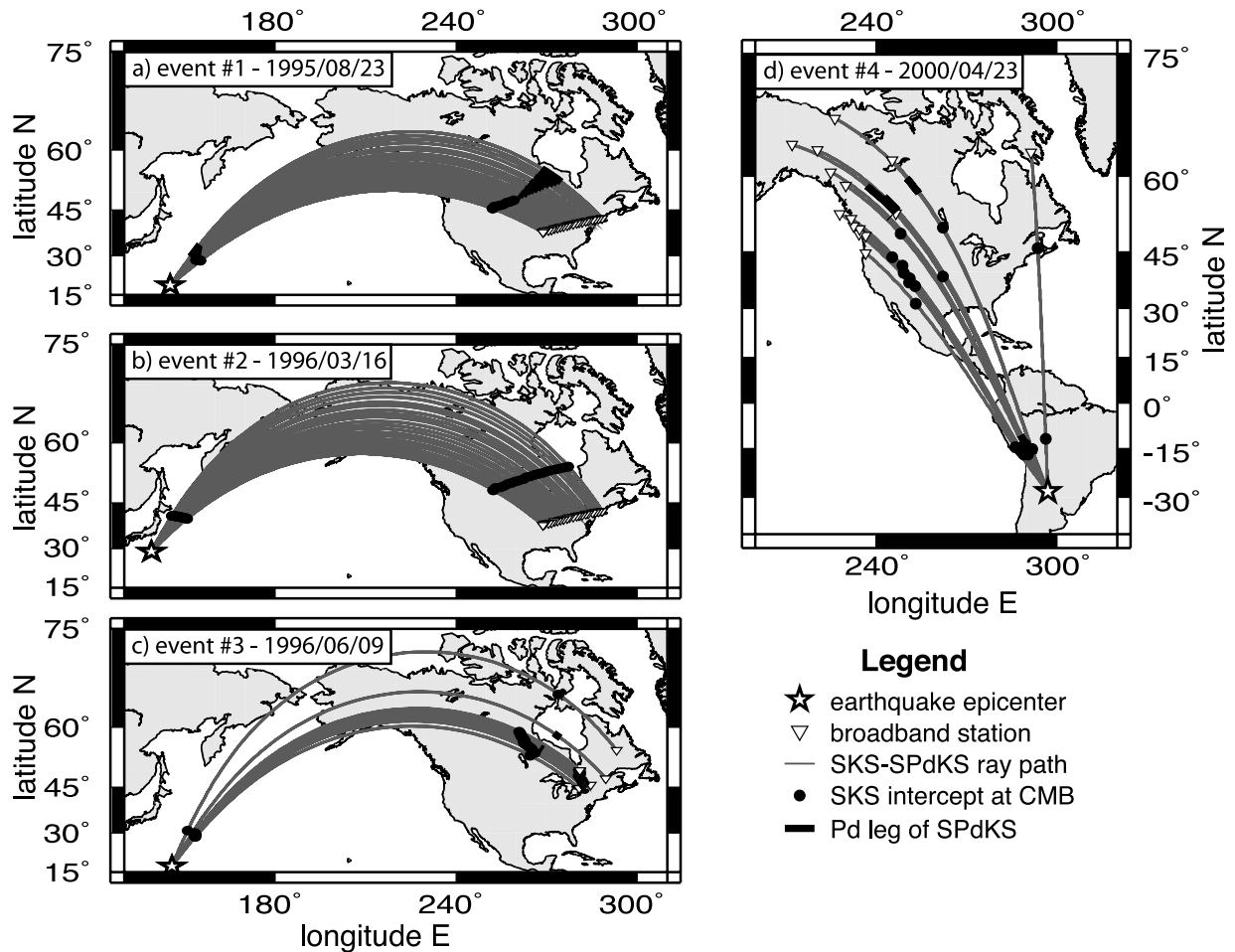


Figure 5. Theoretical *SKS-SPdKS* ray paths for events 1–4, listed in Table 1.

[17] Ultimately, removal of the *SKS* signal by eigenimage processing yields the clearest data section (Figure 6c). The residual section provides an unobstructed view of *SPdKS* from $\sim 109^\circ$ and a set of secondary, coherent phases that are continuous over the entire epicentral distance range, arriving some 5–20 s after *SKS*. The section is reproduced in Figure 7b, with positive pulses shaded in black to emphasize the coherent arrivals. The general trend of *SPdKS* is indicated by a dashed black line and describes an average moveout of 4.5 s° , which is representative of PREM-like velocities at the CMB. The secondary wave field is dominated by a coherent phase composed of two consecutive pulses (c.f., dashed gray lines in Figure 7b) separated by a trough, showing an average moveout of 5.0 s° . Given that these coherent pulses are not observed on either vertical or transverse record sections (not shown here), the moveout is clearly indicative of SV particle motion. To the best of our knowledge, the existence of such a phase in the *SKS* coda has never previously been reported. In analyzing records from the other events, we shall therefore pay particular attention to *SPdKS* waveforms and possible secondary phases in the coda of *SKS*. Accordingly, the dashed lines shown in Figures 7a and 7b will be used as references in the other sections of Figure 7 and for synthetic waveform modeling (section 6).

[18] To verify the robustness of our visual observations, we construct a slant stack map (i.e., vespagram [see, e.g.,

Davies *et al.*, 1971]) from the residual waveform section (Figures 7c, 7f, 7i, and 7l). Localized extrema on the slant stack map help identify and determine the moveout of coherent signal across the waveform section. The map is generated by realigning the traces according to incremental moveouts and stacking them. For N traces of residual waveforms $x'_i(t)$, slant stacking is performed through

$$S(t, p) = \frac{1}{N} \sum_{i=1}^N x'_i(t - \tau_i), \quad (4)$$

with

$$\tau_i = [\Delta_i - \Delta_r]p, \quad (5)$$

where $S(t, p)$ is the amplitude of the stacked traces relative to the normalized *SKS* wavelet, p is the moveout relative to that of *SKS*, Δ_i is the epicentral distance of the i th trace, and Δ_r is the reference distance corresponding to the middle trace of the section. The maximum of the section, $S(t, p)_{\max}$, is shown with a white cross. A 95% confidence interval on this value can be determined with a t test, as the $S(t, p)$ are similar to estimates of a mean. For each point in the map, we construct a sample with $x'_i(t - \tau_i)_{\max} - x'_i(t - \tau_i)$, $i = 1$ to N , and perform a two-tailed t test to verify the hypothesis that this sample's mean is zero, at a 95% confidence level.

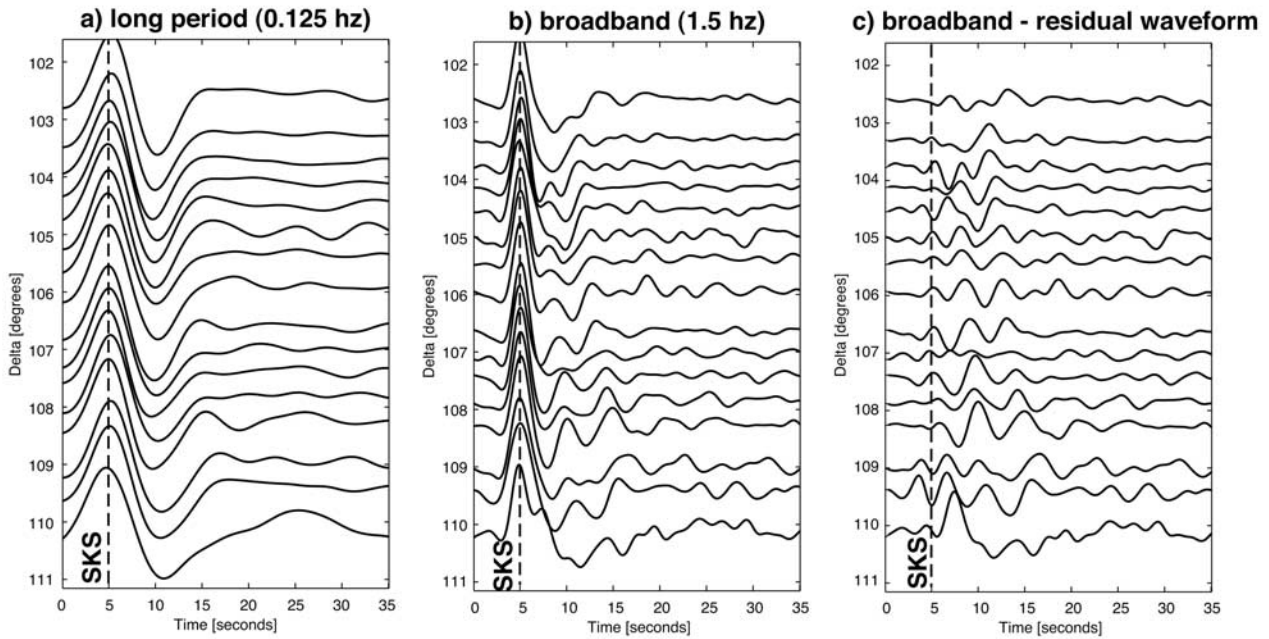


Figure 6. Radial data from event 1 (Table 1), recorded at broadband stations in NE North America. Traces are normalized and aligned with respect to the main *SKS* pulse (centered at 5 s). The three successive sections illustrate how signal in the *SKS* coda can be enhanced by broadening the frequency spectrum from (a) 0.03–0.125 Hz to (b) 0.03–1.5 Hz and (c) by removing the *SKS* waveform with eigenimage processing.

For event 1 (Figure 7c), slant stacking produces a well defined maximum at $t = 13.7$ s and $p = 0.82$ s° , corresponding to a total ray parameter of 5.16 s° , with a confidence interval comprised between 12.6–14.8 s and 0.28–1.20 s° .

5.2. Izu Bonin, 16 March 1996

[19] For this event (event 2 in Table 1), we analyzed records from the same array of broadband stations as in section 5.1 (i.e., MOMA and GSN). The theoretical ray paths for PREM, displayed in Figure 5b, show that the CMB regions sampled by events 2 and 1 are farther apart on the source side than on the receiver side (compare with Figure 5a). The corresponding waveform sections are shown in Figures 7d and 7e. Here, the *SPdKS* wave is not observed over the epicentral distance range covered by the data. However, a secondary phase with moveout similar to that in event 1 (compare with dashed gray lines) is clearly identified between 5 and 14 s over the range 101–103.5°. A vespagram is constructed using the traces comprised in this range (Figure 7f) and shows a well defined maximum at $t = 9.9$ s and $p = 1.30$ s° , with a confidence interval comprised between 9.2–10.6 s and 0.37–1.81 s° . This result implies a total ray parameter of 5.95 s° , a value that is slightly higher than that of the phase observed in event 1. Despite this difference, the two maxima fall in overlapping confidence intervals in terms of their moveout. Note that the difference in t_{\max} between events 1 and 2 reflects the difference in distance sampling of the two events.

[20] In order to further investigate the relationship between the secondary phases observed in events 1 and 2, the residual waveforms from those two events are combined

into a single section, presented in Figure 8. The consolidated section shows that the phase is remarkably continuous across the epicentral distance range 101–110°, thus supporting the hypothesis of a common origin.

5.3. Marianas, 9 June 1996

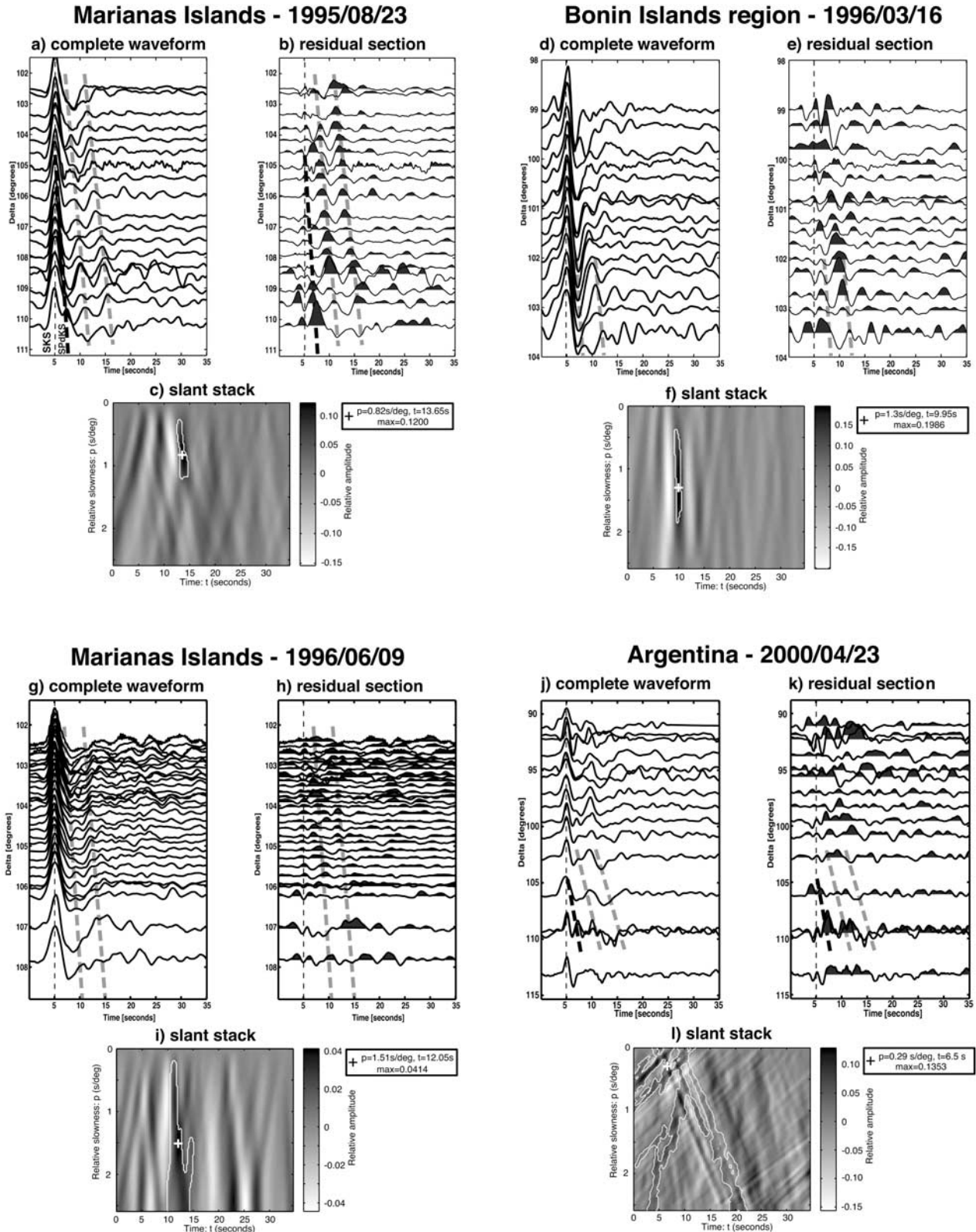
[21] For this second Marianas event (event 3 in Table 1), the waveform section includes records from the IRIS-PASSCAL Abitibi 1996 array [Rondenay *et al.*, 2000], and permanent stations from the CNSN and GSN. The theoretical ray paths for PREM are displayed in Figure 5c, and the corresponding waveform sections are shown in Figures 7g and 7h. Here again, the *SPdKS* wave is not observed over the epicentral distance range covered by the data. However, in contrast to events 1 and 2, there is no strong evidence for a secondary phase in this data section, although a sequence of admittedly weak but coherent pulses between 104 and 108° display a moveout similar to the secondary phase in Figures 7a and 7b (compare with dashed gray lines). Slant stacking of all residual traces (Figure 7i) produces a very low amplitude maximum at $t = 12.0$ s and $p = 1.51$ s° which is poorly defined, as it is characterized by an elongated confidence interval spanning nearly the entire moveout range (i.e., 0.2 to >2.6 s°). Note that, in this case, the CMB regions sampled by events 3 and 1 are nearly identical on the source side but differ on the receiver side (compare Figures 5a and 5c).

5.4. Argentina, 23 April 2000

[22] The last analysis presented in this section was performed on traces recorded by CNSN and GSN permanent station in northwestern North America, for a deep

South American event (event 4 in Table 1). Figure 5d shows the corresponding theoretical ray paths calculated for PREM. Note that these rays provide an overlapping CMB coverage beneath North America with data from events 1–3, while sampling a totally different region on

the source side. The complete and residual waveform sections are presented in Figures 7j and 7k. In this case, *SPdKS* is observed at distances $>109^\circ$ as a positive pulse in the 5–10s time range (see dashed black line), whereas a clear secondary phase is not observed in the *SKS* coda. A



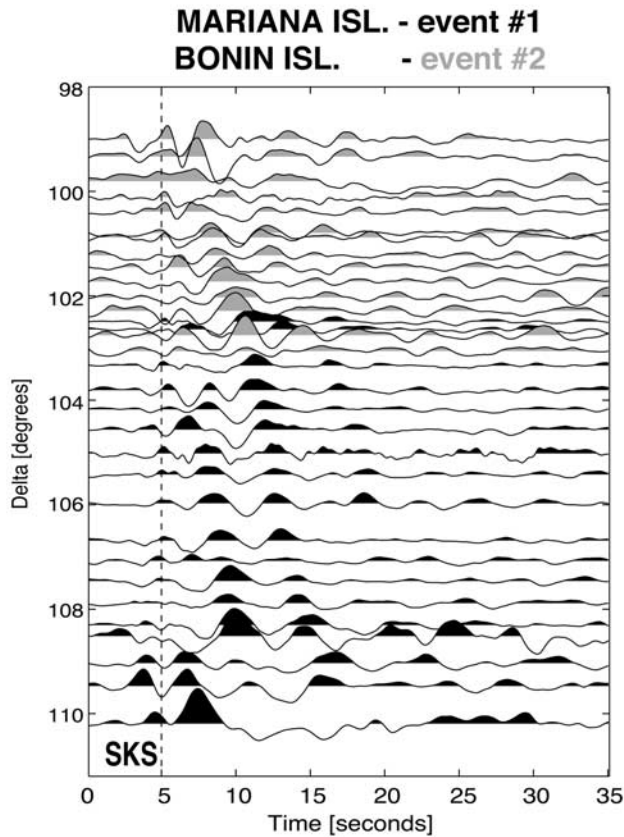


Figure 8. Radial data section combining seismic traces from events 1 (black shading) and 2 (gray shading), listed in Table 1. Traces are normalized and aligned with respect to the main *SKS* pulse (centered at 5 s). Note the continuity of the secondary phase (double pulse between 5 and 20 s) across the epicentral distance range 101° – 110° .

vespagram generated with all the residual traces (Figure 7i) produces a very poorly defined maximum at $t = 6.5$ s and $p = 0.29$ s° , with a confidence interval delineating a complex pattern that spans the entire moveout range and appears to be dominated by noise.

6. Waveform Modeling

[23] The seismic data shown in Figure 7 reveal two significant characteristics of the *SKS-SPdKS* wave field recorded beneath North America. First, *SPdKS* emerges from *SKS* at an epicentral distance of 109° for events in the western Pacific and South America. This corresponds to the theoretical *SPdKS* onset predicted by PREM. Second, a coherent secondary phase is observed between ~ 101

and 110° on selected events recorded by the combined GSN-MOMA array. Note that data sections for other events in the Sea of Japan and SW Pacific recorded at the same array (not shown here) do not manifest the secondary phase, although *SPdKS* phases from SW Pacific events recorded at MOMA do indicate significant ULVZ structure.

[24] In this section, we describe the methodologies employed to model the anomalous *SKS-SPdKS* wave field (including the enigmatic secondary phase) in terms of CMB structure. Synthetic seismograms are computed using the one-dimensional (1-D) reflectivity and generalized ray methods. Whereas modeling techniques have been developed for more complex architectures [see, e.g., *Wen and Helmberger*, 1998a], we chose the 1-D approach as a first step to verify whether simple layered models could produce the observed waveform.

6.1. Origin of Secondary Phase

[25] The assumption that the secondary phase might be generated at the CMB stems from two main observations: first, its close association (in time and epicentral distance) with *SKS* and *SPdKS*; and second, its average moveout of 5.0 s° , which is characteristic of P_{diff} waves sampling lowermost mantle velocities. The robustness of this assumption was evaluated by testing two likely alternatives for the origin of the secondary phase, namely near-surface structure interactions and independent body waves unrelated to *SKS*.

[26] To test the possibility that the secondary phase may have originated at near-surface structure, we investigated synthetic responses for *SKS* conversions and associated surface multiples from velocity discontinuities in the lithosphere. A single, three-dimensional scattering source was not considered given that the moveout of the secondary phase is not representative of realistic *P* or *S* diffractions in the upper ~ 400 km. The synthetic traces were therefore computed with the method of *Frederiksen and Bostock* [2000], which allows for the treatment of dipping and anisotropic planar discontinuities. Using this approach, the secondary phase of Figure 7b could only be reproduced by introducing a uniformly dipping layer extending beneath the entire length of the composite array (Figure 5a). In this case, the arrival that most resembles the secondary phase corresponds to the first free-surface multiple of the discontinuity, $SKS_{fs}S_dS$, where subscripts *fs* and *d* indicate interaction with the free surface and discontinuity, respectively. However, the required extent, depth range (~ 5 – 14 km from western to eastern end of the line) and impedance contrast ($\sim 55\%$) of the discontinuity are not consistent with constraints on crustal structure from *Ps* or active source studies [*Braille*, 1989; *Li et al.*, 2002]. If such a discontinuity did exist, it should produce distinctive *Ps* scattering, and no such phases were observed at MOMA stations [*Li et al.*, 2002]. In

Figure 7. (opposite) Radial data sections for events 1–4, listed in Table 1: (a, d, g, j) complete waveforms and (b, e, h, k) residual waveforms. Traces are normalized and aligned with respect to the main *SKS* pulse (centered at 5 s; see thin dashed lines). The dark and gray dashed lines outline the moveout of *SPdKS* and the secondary phase for event 1 (Figures 7a and 7b), respectively, and serve as references for comparison in subsequent data sections (Figures 7d, 7e, 7g, 7h, 7j, 7k, 9c, and 10c). Note that the secondary phase is clearly observed only in the data sections for events 1 (Figures 7a and 7b) and 2 (Figures 7d and 7e). (c, f, i, l) Slant stacks constructed from the residual waveforms, with incremental slowness increases relative to *SKS*. Maxima are indicated by white crosses, with highlighted areas representing the 95% confidence interval. Well-defined maxima are obtained only for events 1 and 2.

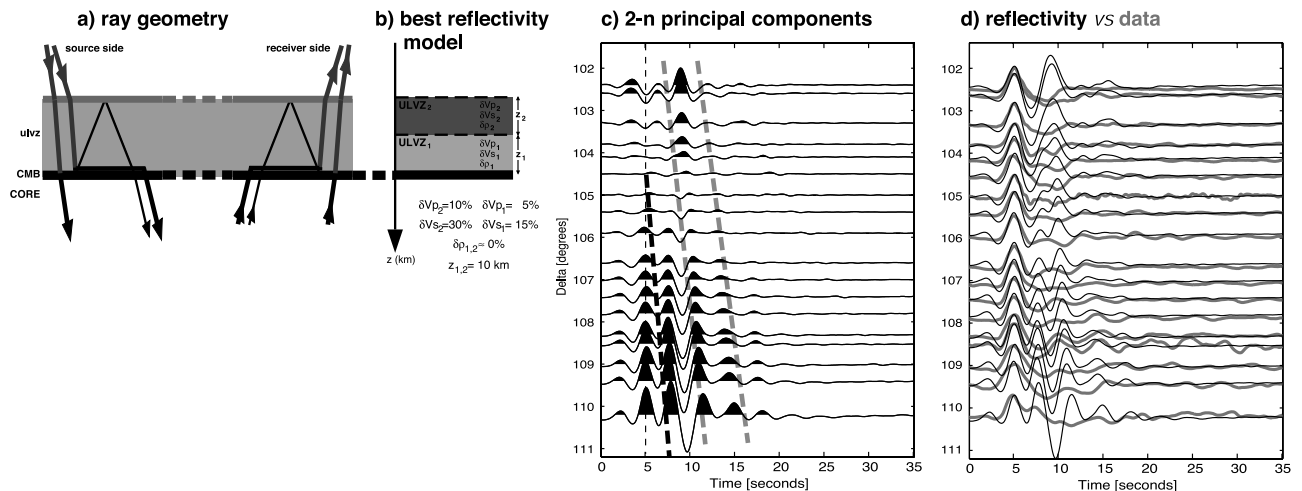


Figure 9. Forward modeling of *SPdKS* and secondary phase using the reflectivity method. (a) ULVZs are modeled as discrete layers with sharp upper and lower boundaries, that are present on both source- and receiver-side CMB intercepts. Downgoing and upgoing rays interact with the upper boundary to create converted phases and multiples that contribute to the distortion of *SPdKS*. (b) Best reflectivity model consisting of two uniform ULVZs, with a top layer characterized by lower velocities than the bottom one. (c) Residual synthetic waveform, with moveouts of *SPdKS* and secondary phase from Figures 7a and 7b indicated by black and gray dashed lines, respectively. Note that because of the complexity of the waveforms and the strong coherence of multiples, eigenimage processing does not entirely strip the *SKS* phase from the section. (d) Comparison between complete synthetic waveform (thin black lines) and the complete waveform from event 1 (thick gray lines; from Figure 7a). Average correlation coefficients for the complete and residual waveforms are 0.32 and -0.15 , respectively.

addition, a discontinuity would be detected on most *SKS* record sections for the MOMA-GSN array, which is not the case. We therefore conclude that the secondary phase does not likely originate at near-receiver structure.

[27] The possibility that the secondary phase might in fact be a body wave unrelated to *SKS* was tested using two approaches. First, we generated full waveform synthetics in the $95\text{--}130^\circ$ distance range using the 1-D reflectivity method [Fuchs and Müller, 1971] (see also section 6.2) for general PREM architecture. The results did not produce any wave resembling the secondary phase. Second, we computed tau-*p* arrival times and ray parameters for a variety of ray paths. A strong constraint on the ray is dictated by the average moveout of the secondary phase (i.e., ~ 5.0 s/ $^\circ$), a value which implies body waves turning in the lower mantle or outer core for *P* waves and in the inner core for *S* waves. Omitting waves that undergo multiple *P-S* or *S-P* conversions at second order discontinuities, we did not find any body wave that satisfied these constraints and displayed the same characteristics as the secondary phase. On the basis of these results, we conclude that the secondary phase is unlikely to represent an independent body wave.

[28] Other, more complex (i.e., 3-D) structure along the ray path has not been considered here and cannot be ruled out as a possible source for the secondary phase. However, evidence pointing to a CMB origin is strong enough to warrant further investigation in that direction.

6.2. Reflectivity Synthetics

[29] The first tool employed to model the anomalous *SKS-SPdKS* waveform of Figures 7a, 7b, and 8 is the

reflectivity method [Fuchs and Müller, 1971]. The method involves the integration, in Fourier domain, of the reflectivity matrix over a range of possible slownesses. The input model is one-dimensional and the resulting waveform includes all possible reflected, transmitted and horizontally refracted rays.

[30] As with previous reflectivity modeling aimed at CMB structure (see Garnero *et al.* [1998] for a review), we treat ULVZs as discrete layers with sharp upper and lower interfaces. Such sharp discontinuities are required in the generation of conversions and multiple reverberations that have been inferred as a major source of *SPdKS* distortion. Furthermore, the reflectivity code employed in this and earlier studies (a descendant of the original program by Fuchs and Müller [1971]) only allows for symmetric models on both source- and receiver-side CMB intercepts (see Figure 9a). The source used to generate the synthetic waveforms consists of a displacement pulse and a double-couple representing event 1, with the following fault plane solution: strike 136° , dip 42° , and slip -118° (Harvard CMT catalog).

[31] Our initial investigations concentrated on single-layered ULVZs with variable thicknesses and velocity contrasts. Ensuing results were comparable to those obtained by Garnero and Helmberger [1998] but did not contain the post-*SKS* ringing characteristic of the secondary phase. We therefore elected to investigate more complex ULVZ architectures involving multiple low-velocity layers stacked above the CMB. The rationale behind such a model was that various sharp boundaries might generate enough reverberations to reproduce the multiple pulses and troughs of the secondary phase, as observed in the residual section

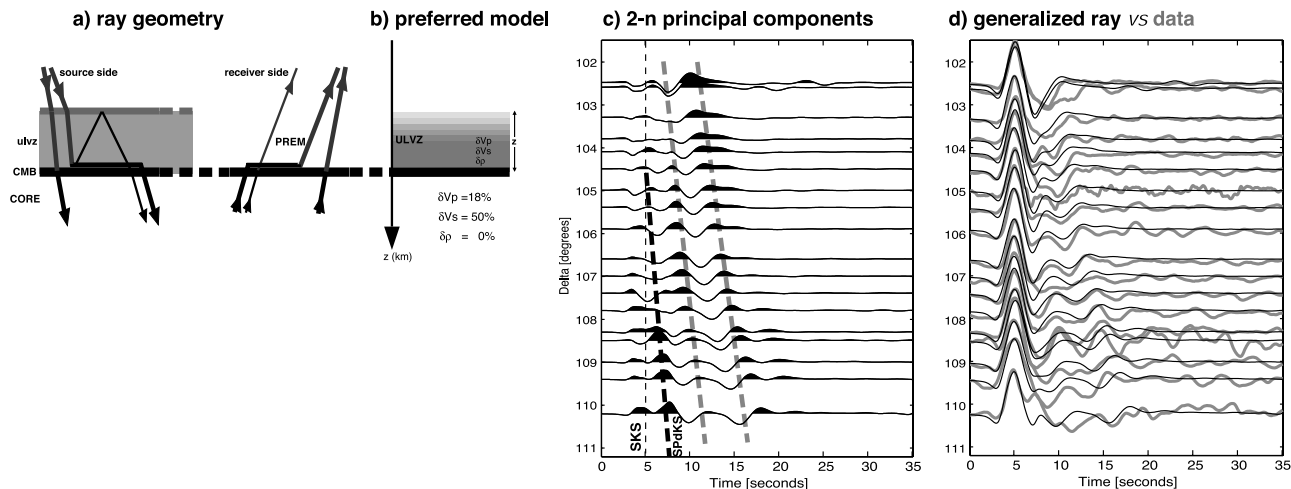


Figure 10. Forward modeling of *SPdKS* and secondary phase using the generalized ray method. (a) ULVZs are modeled as discrete layers with sharp or diffuse upper interface (lower interface stays sharp). The layers can be present on source- and/or receiver-side CMB intercepts, thus allowing for asymmetric structure. (b) Preferred model consisting of a single ULVZ, with a gradational upper boundary. (c) Residual synthetic waveform, with moveouts of *SPdKS* and secondary phase from Figures 7a and 7b indicated by black and gray dashed lines, respectively. (d) Comparison between complete synthetic waveform (thin black lines) and the complete waveform from event 1 (thick gray lines; from Figure 7a). Average correlation coefficients for the complete and residual waveforms are 0.88 and 0.41, respectively.

of Figure 7b. Model space was investigated by varying the number of layers (2–4), layer thicknesses (2–15 km) and velocity perturbations ($\delta V_p = 5\text{--}20\%$, $\delta V_s = 15\text{--}50\%$). The quality of the waveform fits was assessed visually by comparing recorded and synthetic waveforms (i.e., number of pulses, moveout), and quantitatively through the average correlation coefficient between recorded and synthetic waveforms.

[32] Using this approach, we obtained a set of best fitting reflectivity synthetics for a model consisting of two uniform ultralow-velocity layers, superimposed directly above the CMB. The model is described in Figure 9b, with corresponding residual and complete data waveforms shown in Figures 9c and 9d. Note that the best fit is achieved with a stronger velocity reduction in the upper layer, thus implying a negative, upward velocity gradient above the CMB. The residual section (Figure 9c) contains coherent arrivals in the *SKS* coda that resemble both *SPdKS* and the secondary phase (compare with dashed gray lines from Figures 7a and 7b). However, even for the best fitting reflectivity model, the complete synthetic waveform (thin black lines in Figure 9d) contains important precursors and postcursors to *SKS* that are not observed in the real data (thick gray lines). Precursors are related to *S*-to-*P* conversions at the top of the ULVZ, whereas postcursors are generated by multiple reverberation within the ULVZ [see, e.g., *Garnero and Helmberger, 1998*]. Since these features are not present in the recorded data, we conclude that the model of Figure 9 is not a viable candidate to explain the secondary phase.

[33] This example illustrates the numerous, unsuccessful attempts that were made at modeling the secondary phase with the reflectivity method. We consistently found that the level of complexity in CMB structure necessary to fit the residual waveform produced large arrivals in the

complete synthetic waveform that do not appear in the data.

6.3. Generalized Ray

[34] The generalized ray technique was also employed to model the anomalous *SKS-SPdKS* waveforms. The method was originally developed by *Cagniard* [see *Cagniard, 1962*], and later simplified by *de Hoop* [1960]. It was adapted for propagation of seismic waves through stratified media by *Helmberger* [1968] (see also *Aki and Richards* [2002] for a review). This method produces synthetic waveforms by solving the elastic wave equation for individual, prescribed rays in a 1-D layered Earth. The approach has been previously applied to ULVZ modeling by *Helmberger et al.* [1996] and *Wen and Helmberger* [1998a]. Here, we employ a modified version of the program developed in the former paper, where ULVZs are treated as discrete layers with either a sharp or diffuse upper interface and a sharp lower boundary at the CMB. The algorithm allows for the treatment of asymmetric structure between source- and receiver-side CMB intercepts (Figure 10a). Synthetic waveforms are generated by convolving the displacement potential, which is output by the program, with appropriate source time function and instrument response. Here, we convolve the output with the *SKS* estimate obtained for event 1 (i.e., first eigenmode of data section in Figure 7a).

[35] A variety of models including single and double ULVZs with different thicknesses (2–15 km) and velocity perturbations ($\delta V_p = 5\text{--}20\%$, $\delta V_s = 15\text{--}50\%$) were tested using generalized ray synthetics. Resulting waveforms showed that the anomalous waveforms in Figures 7a–7f could not be explained with any combination of symmetric or asymmetric ULVZs that contained sharp upper boundaries. Wave conversions and multiples arising from sharp ULVZ upper boundaries create *SKS* precursors and post-

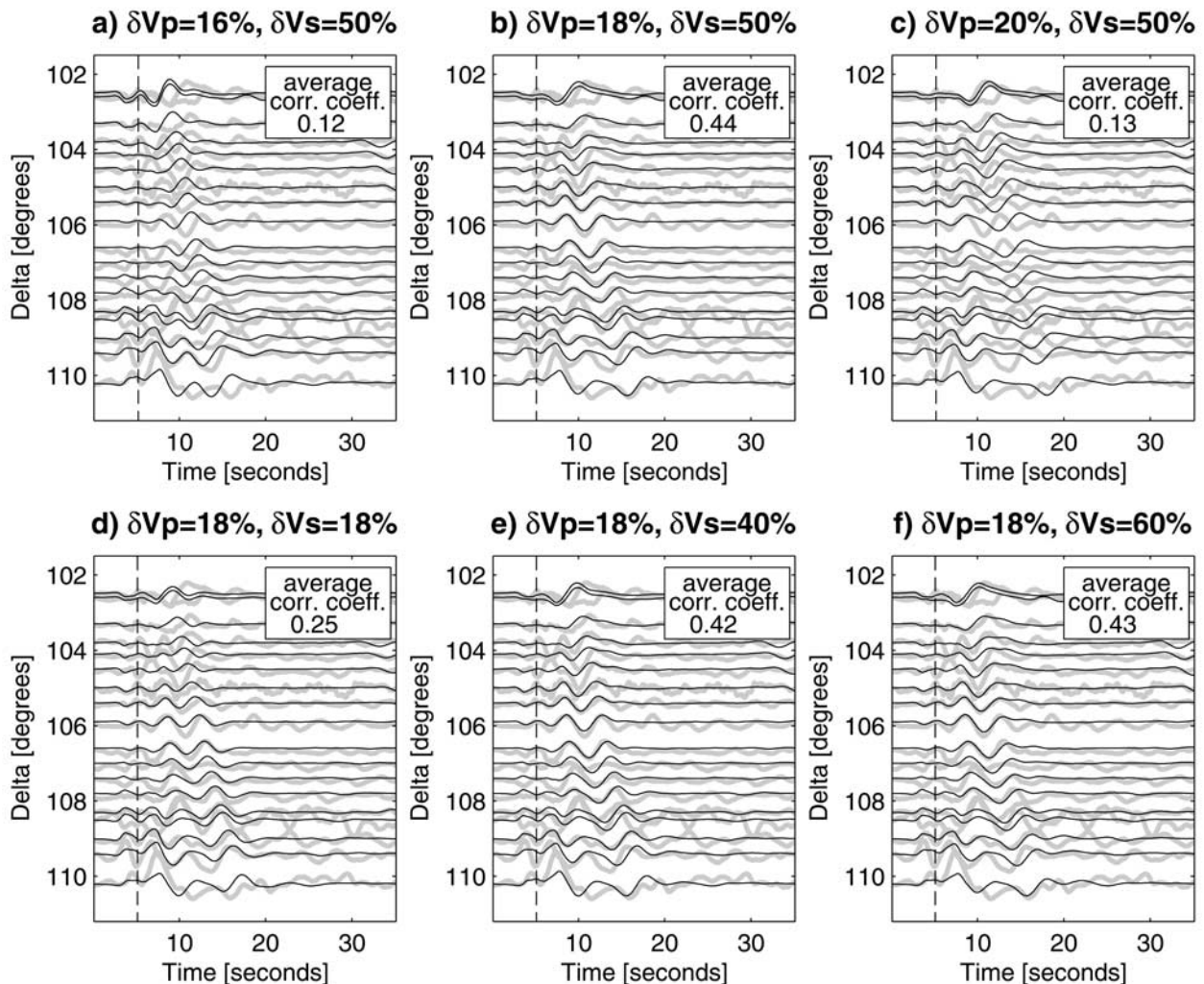


Figure 11. Effects on waveform fits of small changes in δV_p and δV_s from the preferred model in Figure 10. The sections show comparisons between the residual waveform from event 1 (thick gray lines) and generalized ray synthetics (thin black lines). Average correlation coefficients between real and synthetic waveforms are given in the insets. (b) Preferred model is shown. (a and c) A δV_p variation $\geq 2\%$ produce significant deterioration of the waveform fit, resulting in improper alignment of the secondary phases and important reductions in average correlation coefficients. (d–f) Conversely, the waveforms are not as sensitive to δV_s variations, where changes $>15\text{--}20\%$ are necessary to lower the quality of the fit.

cursors that are not observed in the broadband data. To reduce synthetic waveform complexity, a diffuse upper boundary was simulated by eliminating contributions from all the rays that interact with the upper boundary. Our preferred model, which is presented in Figure 10b, was obtained by varying the parameters of such simple ULVZ architecture. The model consists of PREM-like CMB velocities on one side of the *SPdKS* path and a single ULVZ on the other side, with large velocity perturbations of 18% and 50% for *P* and *S* waves, respectively. Note that the synthetic data section obtained after eigenimage processing (Figure 10c) contains coherent phases that closely resemble *SPdKS* and the secondary phase observed in Figure 7b. Furthermore, the complete synthetic waveform (Figure 10d) fits the data of Figure 7a remarkably well, with an average

correlation coefficient of 0.88. Close inspection of the synthetic displacement potentials (not presented here) shows that the secondary phase is related, in this case, to a decoupling between source- and receiver-side *SPdKS* waves. Specifically, the ULVZ side of the path produces an *SPdKS* emerging at $\sim 95^\circ$ with a moveout of 5.40 s° , whereas the PREM side produces one which emerges at $\sim 105^\circ$ with a moveout of 4.43 s° . The complex ringing of the secondary phase is associated with interference patterns of the *SKS*, *SPdKS*, and *SKPdS* impulse responses.

[36] To assess the robustness of our preferred model parameters, we first investigate the effects of independent variations in δV_p and δV_s on the residual waveform fits (see Figure 11). Changes in δV_p modify the moveout of the

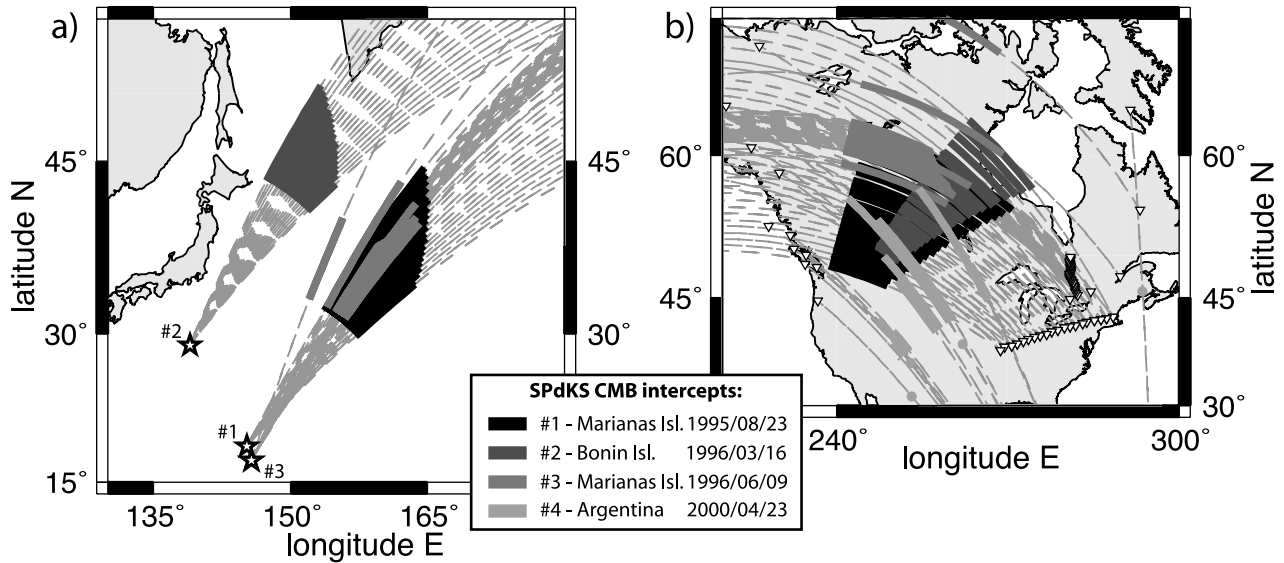


Figure 12. Combined CMB intercepts of *SPdKS* waves calculated for the preferred model with $\delta V_p = 18\%$ and $\delta V_s = 50\%$. (a) Map of the SW Pacific showing source-side CMB intercepts for events 1–3. (b) Map of North American showing receiver-side CMB intercepts for events 1–4.

secondary phase, whereas changes in both δV_p and δV_s control the onset of the phase. We note that δV_p variations $\geq 2\%$ from that of the preferred model produce significant deterioration of the waveform fit, resulting in improper alignment of the secondary phases and important reductions in average correlation coefficient (compare Figures 11a and 11c with preferred model in Figure 11b). Values of δV_s are not as well constrained as those of δV_p , as only changes $>15\text{--}20\%$ significantly affect the waveform fit (see Figures 11d–11f). Note that for a $\delta V_p:\delta V_s$ ratio of 1:1 with 18% reduction (Figure 11d), the waveform fit is compromised mainly in the lower epicentral distances, between 102 and 106° . Further testing with the 1:1 ratio and variable velocity reductions did not produce any acceptable waveform fit.

[37] In contrast to velocities, ULVZ thickness and density perturbations remain only loosely constrained with generalized ray synthetics. To better constrain the upper boundary gradient, we compared reflectivity and generalized ray synthetics for symmetric ULVZs with velocity perturbations as those of our preferred model. Results from this exercise were not conclusive, as the P_{diff} waveform generated by reflectivity synthetics becomes unstable when attempting to simultaneously include higher frequencies (>0.1 Hz) and simulate a diffuse boundary with a large number of very thin (<1 km) layers. In addition, the inclusion of higher frequencies requires artificially low attenuation (i.e., high Q) in the lower mantle (E. Garnero and M. Thorne, personal communication, 2002). This nonideal treatment of Q causes further discrepancies between generalized ray and reflectivity modeling of the diffuse boundary. Despite these limitations, we note that *SKS* precursors generated by reflectivity disappear for a diffuse boundary with thickness $>20\text{--}30$ km, a value which we retain as a minimum thickness for our preferred gradational ULVZ. The density, which determines the impedance contrast of the upper boundary, is poorly constrained since wave interactions with that discontinuity are not considered in the final model.

[38] In summary, our preferred model consists of a single asymmetric ULVZ located on either source- or receiver-side CMB intercept. The layer has a thickness of at least $20\text{--}30$ km, with a diffuse upper boundary and maximum P and S velocity perturbations of 18% and 50% , respectively.

7. Discussion

[39] We now interpret the preferred model of section 6.3 in terms of regional processes taking place in the lowermost mantle and at the CMB. The first challenge is to clarify the fundamental ambiguity between source- and receiver-side ULVZs, as the two possible locations produce the same theoretical waveform. Important information pertaining to this problem is obtained from the CMB intercepts of *SPdKS* waves, as calculated for our preferred model with $\delta V_p = 18\%$ and $\delta V_s = 50\%$. Corresponding P_{diff} segments beneath the western Pacific and North America for the events of Table 1 are presented in Figure 12. For signal in the $5\text{--}10$ s period range and a fixed distance of inception, P_{diff} segments have a Fresnel zone half width of $\sim 160\text{--}240$ km in the direction perpendicular to the ray (transverse) and $20\text{--}35$ km in the direction parallel to the ray (longitudinal). These values can provide a rough estimate of the lateral resolution afforded by rays sampling the CMB, although recent studies have shown consistent waveform variations occurring over transverse CMB scale lengths <100 km [see, e.g., Wen, 2001].

[40] In our investigations, we noted that the secondary phase was clearly observed solely on record sections from events 1 and 2 (Figure 7). The two sets of rays sample regions of the CMB that are significantly different on the source side, where respective coverage areas are separated by ~ 700 km (i.e., a distance significantly greater the Fresnel zone), but overlap almost entirely on the receiver side (see Figure 12). In contrast, the secondary phase is not clearly observed on records from event 3, whose rays nearly coincide with those of event 1 beneath the Pacific, but not

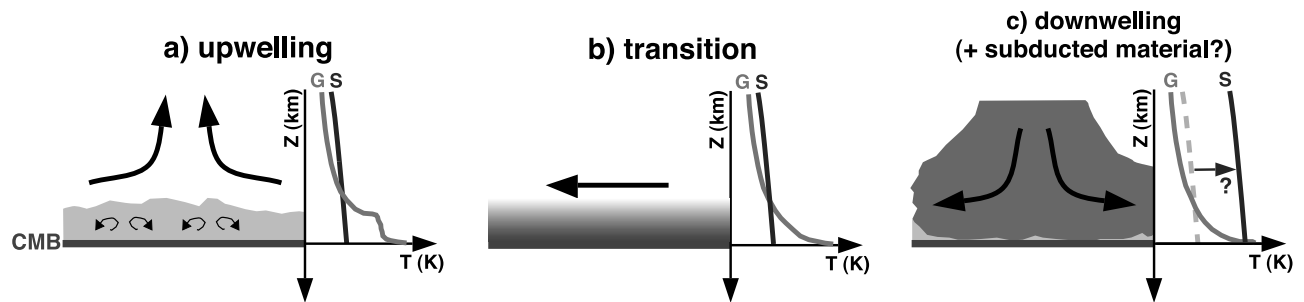


Figure 13. Schematic representation of laterally varying CMB domains. G, geotherm; S, solidus of lowermost mantle materials. The CMB region underlying central North America, where a diffuse ULVZ (b) is inferred to be a transition between (a) regions of mantle upwelling, where sharp ULVZs may be present, and (c) regions of mantle downwelling, where ULVZs are either nonexistent or imperceptibly thin. See text for details.

beneath North America. On the source side, the distance between respective mantle-CMB intercepts for events 1 and 3 is <20 km, which is less than the longitudinal Fresnel zone. On the receiver side, the CMB patches sampled by the two events partly overlap, although the core-CMB intercepts (i.e., the points where receiver-side *SPdKS* are generated) differ by more than 120–150 km, well above the longitudinal Fresnel zone. Note that the comparisons between events 1, 2, and 3 are consistent with the results from all the other events that were investigated. In light of these observations, we infer that the diffuse ULVZ is more likely to be located beneath North America than the western Pacific. On the basis of this assumption, westward variations in CMB structure beneath North America, as implied by the waveforms from event 3, might be related to the change in ULVZ response previously reported in the region by *Garnero et al.* [1998] (see Figure 4). Records from South American events (e.g., event 4) sample regions of the CMB farther to the south beneath North America and do not contain the secondary phase. These results are therefore used to determine the southern boundary of the diffuse ULVZ region.

[41] The inferred regional extent of the diffuse ULVZ is outlined in Figure 4a, along with the global ULVZ distribution of *Garnero et al.* [1998]. The shape of the diffuse layer region is based on the distribution of rays that generate the secondary phase and their associated Fresnel zones. As noted in section 4, previously identified ULVZs were correlated with low-velocity regions in the lowermost mantle, whereas a PREM-like CMB architecture was assumed to prevail in faster regions. In contrast, the diffuse ULVZ inferred here appears to be associated with nearly neutral *S* velocities over the depth interval 2650–2890 km (compare with Figure 4b).

[42] To better assess the implication of a ULVZ embedded at the base of a zone of neutral CMB velocity, we briefly review petrological and geodynamic models that have been proposed in relation to global ULVZ distribution. In general, the CMB is assumed to be isothermal, with a temperature in the range 2500–4500 K on the mantle side (D'') and a superadiabatic increase of ~ 1000 – 2000 K from mantle to core [Williams, 1998]. The average pressure at CMB depths is ~ 130 GPa. High-pressure experiments indicate that, at these conditions, the solidus of lower mantle

minerals (perovskite and magnesiowüstite) can intersect the geotherm, thus leading to the production of partial melt [Holland and Ahrens, 1997]. Results by *Knittle* [1998] suggest that the iron might preferentially fractionate into the liquid phase, favoring a melt that is denser than the solid residual. It is these observations, coupled with the preferred $\delta V_p:\delta V_s$ ratio of 1:3, that have led to the interpretation of ULVZs as layers of partial melt [Williams and Garnero, 1996; Revenaugh and Meyer, 1997; Berryman, 2000].

[43] In this context, two end-term models have been suggested to explain the lateral variability of ULVZ observations [Garnero et al., 1998]. First, well-defined ULVZs are associated with regions of large scale mantle upwelling, such as that beneath the Pacific superplume. In such regions, higher temperatures in the lower mantle may lead to more abundant partial melt and possible localized convection in the ULVZ, as schematically shown in Figure 13a (based on Figure 10 of *Garnero et al.* [1998]). Second, CMB regions that lack evidence for ULVZs may be associated with mantle downwelling. These regions generally display lower mantle temperatures and many have been the target of advected material from subducted slabs over 100–200 Myr timescales. In this case, which is schematically shown in Figure 13c (also based on Figure 10 of *Garnero et al.* [1998]), ULVZs may be very thin due to the following factors: (1) lower temperatures, (2) mantle downwelling, and (3) decrease in melt buoyancy or shifting of the solidus due to advected material. Such compositional modulation of the melting potential at the CMB has been suggested by *Wen et al.* [2001] to explain small-scale, lateral variations in ULVZ structure.

[44] In light of the CMB models presented above, we interpret the ULVZ we observe beneath North America to be a transition zone laterally separating downwelling from upwelling domains. Such transition zones may be associated with regions of average temperatures/composition in the lowermost mantle, where ULVZs remain stable and contain increasing amounts of partial melt with proximity to the CMB (Figure 13b). On the basis of the calculations of *Williams and Garnero* [1996], the inferred velocity perturbations $\delta V_p = 18\%$ and $\delta V_s = 50\%$ could indicate a melt fraction ranging between ~ 15 and 45% depending on the melt geometry. The increase in melt percent with depth within the ULVZ could be explained by two processes: first, a steady

increase in temperature, and second, unperturbed gravitational sinking of Fe-rich melt, unhindered by localized, small-scale convection as in Figure 13a. Therefore, if temperature fluctuations are the main cause for lateral ULVZ variability, our interpretation supports the suggestion of *Revenaugh and Meyer* [1997] that ULVZs may be a ubiquitous phenomenon, only with regional characteristics that render them more or less detectable by seismic methods. Alternatively, if compositional anomalies significantly modulate the distribution of partial melt, they could also explain why ULVZs are laterally intermittent features of the lower mantle [see, e.g., *Wen et al.*, 2001]. In this case, the transitional ULVZ we observe beneath North America could represent a chemical gradient or a more complex interaction between chemical and thermal anomalies.

8. Concluding Remarks

[45] In this study, we have shown that a recent increase in spatial density of broadband seismic data can greatly improve SKS coda analysis for CMB imaging purposes. The richer spectral content of the signal allows for better detection of SPdKS and other coherent phases generated by CMB structure. Furthermore, its higher spatial density renders the data amenable to multichannel signal processing approaches. Here, we have developed an eigenimage decomposition algorithm that effectively isolates the phases of interest from the SKS waveform.

[46] Applying this approach to North American broadband data, a coherent secondary phase was identified in the SKS coda on paths sampling the CMB beneath North America. Using 1-D asymmetric modeling approaches, the phase could be reproduced by introducing a ULVZ above the CMB on one side of the SPdKS path. This model was found to be valid only if the upper boundary of the ULVZ was diffuse enough to prevent the generation of significant reflections and conversions. It is important to note, however, that although the anomalous SKS-SPdKS waveform could be explained with a simple 1-D architecture, one cannot exclude the contribution from more complex (i.e., 2-D, on- and off-azimuth 3-D) structure. The investigation of complex structure is the topic of ongoing research, which should greatly benefit from further improvement in broadband data coverage (e.g., USArray, *Levander et al.* [1999]), and the recent development of full 3-D modeling approaches [e.g., *Komatitsch et al.*, 2002]. Nevertheless, our preferred model is physically plausible. It suggests that laterally variable and vertically diffuse ULVZs may be a characteristic of transitional CMB domains that lie between regions of mantle upwelling, where ULVZs are more uniformly observed, and regions of downwelling, where ULVZs are either nonexistent or imperceptibly thin.

[47] **Acknowledgments.** We thank Ed Garnero, Lianxing Wen, Sebastian Rost and Justin Revenaugh for stimulating discussions, help with the codes, and their constructive reviews of the original manuscript. We also thank Don Helmberger and Ken Creager for helpful discussions. We thank the IRIS DMC, and the Geological Survey of Canada for access to the North American broadband data; IRIS PASSCAL for support of the MOMA and, along with Lithoprobe, the Abitibi experiments. We also wish to acknowledge the researchers and students who made these two experiments possible; Julie Zaslow, who conducted an early SPdKS analysis on MOMA waveforms; Andrew Frederiksen, for his modeling

code; and Steve Grand, for providing his tomographic model. S. R. wishes to thank Ken Creager for his hospitality at UW. The authors made use of the Generic Mapping Tool [*Wessel and Smith*, 1995] for some figures. This research was supported by an NSERC Postdoctoral Fellowship to S. R. and NSF grant EAR-9903385.

References

Aki, K., and P. G. Richards, *Quantitative Seismology*, 2nd ed., Univ. Sci. Books, 700 pp., Sausalito, Calif., 2002.

Berryman, J. G., Seismic velocity decrement ratios for regions of partial melt in the lower mantle, *Geophys. Res. Lett.*, 27, 421–424, 2000.

Braile, L. W., Crustal structure of the continental interior, in *Geophysical Framework of the Continental United States*, edited by L. C. Pakiser and W. D. Mooney, *Mem. Geol. Soc. Am.*, 172, 285–315, 1989.

Buffett, B. A., E. J. Garnero, and R. Jeanloz, Sediments and the top of Earth's core, *Science*, 288, 2007–2012, 2000.

Cagniard, L., *Reflection and Refraction of Progressive Seismic Waves*, translated by E. A. Flinn and C. H. Dix, McGraw-Hill, New York, 1962.

Choy, G. L., Theoretical seismograms of core phases calculated by frequency-dependent full wave theory, and their interpretation, *Geophys. J. R. Astron. Soc.*, 51, 275–312, 1977.

Davies, D., E. J. Kelly, and J. R. Filson, Vespa process for analysis of seismic signals, *Nature Phys. Sci.*, 232, 8–13, 1971.

de Hoop, A. T., A modification of Cagniard's method for solving seismic pulse problems, *Appl. Sci. Res., Ser. B*, 8, 349–356, 1960.

Dziewonski, A. M., and D. L. Anderson, Preliminary reference Earth model (PREM), *Phys. Earth Planet. Inter.*, 25, 297–356, 1981.

Frederiksen, A. W., and M. G. Bostock, Modelling teleseismic waves in dipping anisotropic structures, *Geophys. J. Int.*, 141, 401–412, 2000.

Fuchs, K., and G. Müller, Computation of synthetic seismograms with the reflectivity method and comparison with observations, *Geophys. J. R. Astron. Soc.*, 23, 417–433, 1971.

Garnero, E. J., and D. V. Helmberger, A very slow basal layer underlying large-scale low-velocity anomalies in the lower mantle beneath the Pacific—evidence from core phases, *Phys. Earth Planet. Inter.*, 91, 161–176, 1995.

Garnero, E. J., and D. V. Helmberger, Seismic detection of a thin laterally varying boundary layer at the base of the mantle beneath the central-Pacific, *Geophys. Res. Lett.*, 23, 977–980, 1996.

Garnero, E. J., and D. V. Helmberger, Further structural constraints and uncertainties of a thin laterally varying ultralow-velocity layer at the base of the mantle, *J. Geophys. Res.*, 103, 12,495–12,509, 1998.

Garnero, E. J., and R. Jeanloz, Fuzzy patches on the Earth's core-mantle boundary?, *Geophys. Res. Lett.*, 27, 2777–2780, 2000.

Garnero, E. J., S. P. Grand, and D. V. Helmberger, Low P-wave velocity at the base of the mantle, *Geophys. Res. Lett.*, 20, 1843–1846, 1993.

Garnero, E. J., J. S. Revenaugh, Q. Williams, T. Lay, and L. H. Kellogg, Ultralow velocity zone at the core-mantle boundary, in *The Core-Mantle Boundary Region*, *Geodyn. Ser.*, vol. 28, edited by M. Gurnis et al., pp. 319–334, AGU, Washington, D. C., 1998.

Grand, S. P., Mantle shear-wave tomography and the fate of subducted slabs, *Philos. Trans. R. Soc. London*, 360, 2475–2491, 2002.

Helmberger, D. V., The crust-mantle transition in the Bering Sea, *Bull. Seismol. Soc. Am.*, 58, 179–214, 1968.

Helmberger, D. V., Theory and application of synthetic seismograms, in *Earthquakes: Observations, Theory, and Interpretation*, edited by H. Kanamori and E. Boschi, pp. 174–222, North-Holland, New York, 1983.

Helmberger, D. V., E. J. Garnero, and X. Ding, Modeling two-dimensional structure at the core-mantle boundary, *J. Geophys. Res.*, 101, 13,963–13,972, 1996.

Holland, K. G., and T. J. Ahrens, Melting of (Mg, Fe)₂SiO₄ at the core-mantle boundary of the Earth, *Science*, 275, 1623–1625, 1997.

Knittle, E., The solid/liquid partitioning of major and radiogenic elements at lower mantle pressures: Implications for the core-mantle boundary region, in *The Core-Mantle Boundary Region*, *Geodyn. Ser.*, vol. 28, edited by M. Gurnis et al., pp. 119–130, AGU, Washington, D. C., 1998.

Knittle, E., and R. Jeanloz, Simulating the core-mantle boundary: An experimental study of high-pressure reactions between silicates and liquid iron, *Geophys. Res. Lett.*, 16, 609–612, 1989.

Komatitsch, D., J. Ritsema, and J. Tromp, The spectral-element method, Beowulf computing and global seismology, *Science*, 298, 1737–1742, 2002.

Lay, T., Q. Williams, and E. J. Garnero, The core-mantle boundary layer and deep Earth dynamics, *Nature*, 392, 461–468, 1998.

Levander, A., E. Humphreys, G. Ekstrom, A. Meltzer, and P. Shearer, Proposed project would give unprecedented look under North America, *Eos Trans. AGU*, 80, 245, 1999.

- Li, A., K. M. Fischer, S. van der Lee, and M. E. Wysession, Crust and upper mantle discontinuity structure beneath eastern North America, *J. Geophys. Res.*, 107(B5), 2100, doi:10.1029/2001JB000190, 2002.
- Liu, X.-F., and A. M. Dziewonski, Global analysis of shear wave velocity anomalies in the lower-most mantle, in *The Core-Mantle Boundary Region, Geodyn. Ser.*, vol. 28, edited by M. Gurnis et al., pp. 21–36, AGU, Washington, D. C., 1998.
- Masters, G., G. Laske, H. Bolton, and A. Dziewonski, The relative behavior of shear velocity, bulk sound speed, and compressional velocity in the mantle: Implications for chemical and thermal structure, in *Earth's Deep Interior: Mineral Physics and Tomography From Atomic to Global Scale, Geophys. Monogr. Ser.*, vol. 117, edited by S. Karato et al., pp. 63–87, AGU, Washington, D. C., 2000.
- Mori, J., and D. V. Helmberger, Localized boundary layer below the mid-Pacific velocity anomaly identified from a *PcP* precursor, *J. Geophys. Res.*, 100, 20,359–20,365, 1995.
- Revenaugh, J., and R. Meyer, Seismic evidence of partial melt within a possibly ubiquitous low-velocity layer at the base of the mantle, *Science*, 277, 670–673, 1997.
- Rondenay, S., M. G. Bostock, T. M. Hearn, D. J. White, and R. M. Ellis, Lithospheric assembly and modification of the SE Canadian Shield: Abitibi-Grenville Teleseismic Experiment, *J. Geophys. Res.*, 105, 13,735–13,754, 2000.
- Rost, S., and J. Revenaugh, Seismic detection of rigid zones at the top of the core, *Science*, 294, 1911–1913, 2001.
- Ulrych, T. J., M. D. Sacchi, and S. L. M. Freire, Eigenimage processing of seismic sections, in *Covariance Analysis of Seismic Signal Processing, Geophys. Dev. Ser.*, vol. 8, edited by R. L. Kirilin and W. J. Done, Soc. of Explor. Geophys., Tulsa, Okla., 1999.
- van der Hilst, R. D., S. Widiyantoro, K. C. Creager, and T. J. McSweeney, Deep subduction and aspherical variations in *P*-wavespeed at the base of Earth's mantle, in *The Core-Mantle Boundary Region, Geodyn. Ser.*, vol. 28, edited by M. Gurnis et al., pp. 5–20, AGU, Washington, D. C., 1998.
- VanDecar, J. C., and R. S. Crosson, Determination of teleseismic relative phase arrival times using multi-channel cross-correlation and least squares, *Bull. Seismol. Soc. Am.*, 80, 150–159, 1990.
- Wen, L., Seismic evidence for a rapidly-varying compositional anomaly at the base of the Earth's mantle beneath the Indian ocean, *Earth Planet. Sci. Lett.*, 194, 83–95, 2001.
- Wen, L., and D. V. Helmberger, A two-dimensional *P-SV* hybrid method and its application to modeling localized structures near the core-mantle boundary, *J. Geophys. Res.*, 103, 17,901–17,918, 1998a.
- Wen, L., and D. V. Helmberger, Ultra-low velocity zones near the core-mantle boundary from broadband *PKP* precursors, *Science*, 279, 1701–1703, 1998b.
- Wen, L., P. Silver, D. James, and R. Kuehnel, Seismic evidence for a thermo-chemical boundary at the base of the Earth's mantle, *Earth Planet. Sci. Lett.*, 189, 141–153, 2001.
- Wessel, P., and W. H. F. Smith, New version of the Generic Mapping Tools released, *Eos Trans. AGU*, 76, 329, 1995.
- Williams, Q., The temperature contrast across D", in *The Core-Mantle Boundary Region, Geodyn. Ser.*, vol. 28, edited by M. Gurnis et al., pp. 73–81, AGU, Washington, D. C., 1998.
- Williams, Q., and E. J. Garnero, Seismic evidence for partial melt at the base of Earth's mantle, *Science*, 273, 1528–1530, 1996.
- Williams, Q., J. Revenaugh, and E. Garnero, A correlation between ultra-low basal velocities in the mantle and hot spots, *Science*, 281, 546–549, 1998.

K. M. Fischer, Department of Geological Sciences, Brown University, P.O. Box 1846, Providence, RI 02912, USA. (karen_fischer@brown.edu)
 S. Rondenay, Department of Earth, Atmospheric and Planetary Sciences, Massachusetts Institute of Technology, 77 Massachusetts Ave., 54–512, Cambridge, MA 02139, USA. (rondenay@mit.edu)